INDEX COPERNICUS INTERNATIONAL

Bio-Algorithms and Med-Systems

WWW.BAMSJOURNAL.COM ISSN: 1896-530X

ORIGINAL ARTICLE

Received: 03.11.2025
Accepted: 18.11.2025
Published: 23.12.2025

CITE THIS ARTICLE AS:
Tiwari S, Sharma S, Moskal P, "Feasibility Study of Using Detector-Scattered Photons for Attenuation Correction in CT-less PET Imaging," Bio-Algorithms and Med-Systems vol. 21, special issue New Trends in Nuclear and Medical Physics, pp. 13-20, 2025, DOI: 10.5604/01.3001.0055.4655

AUTHORS' CONTRIBUTION:
A – Conceptualization
B – Data Curation
C – Formal Analysis
D – Funding Acquisition
E – Investigation
F – Methodology
G – Project Administration
H – Resources
I – Software
J – Supervision
K – Validation
L – Visualization
M – Writing – Original Draft
N – Writing – Review & Editing

CORRESPONDING AUTHOR:
Satyam Tiwari; Faculty of Physics, Astronomy and Applied Computer Science, Jagiellonian University; Lojasiewicza street 11, 30-348 Kraków, Poland; E-mail: satyam.tiwari@doctoral.uj.edu.pl

Feasibility Study of Using Detector-Scattered Photons for Attenuation Correction in CT-less PET Imaging

Satyam Tiwari[1,2 ABCEFIKLMN], Sushil Sharma[1,2 AEFGHJKN], Paweł Moskal[1,2 ADEGHJKN]

[1]Faculty of Physics, Astronomy and Applied Computer Science, Jagiellonian University, Kraków, Poland
[2]Center for Theranostics, Jagiellonian University, Kraków, Poland

ABSTRACT

Objective: Quantitative PET requires accurate attenuation correction (AC), which is conventionally achieved using CT-derived maps, incurring extra dose and complexity. This study explores a CT-less AC approach for the plastic scintillator-based J-PET scanner by investigating whether detector-scattered photons (DS-LORs) can serve as an intrinsic transmission source.

Methods:

• Simulation Setup: The study utilised GATE v9.1 software to simulate the modular J-PET scanner, which consists of plastic scintillator strips where 511 keV photons predominantly undergo Compton scattering. Two configurations were evaluated: a uniform water cylinder and a NEMA IQ-like phantom containing a cold lung insert and six hot spheres to simulate heterogeneous activity.

• Analysis & reconstruction: The study isolated triple-hit coincidences to analyse angular deviations. DS-LORs were identified using a specific scatter test metric based on interaction positions and detection times. Attenuation maps were reconstructed using Filtered Back Projection (FBP) applied to the ratio of water-to-air sinograms.

Results: Due to the properties of plastic scintillators, DS-LORs constituted approximately 50% of all detected prompts, providing a substantial dataset for analysis. In a simulated 10-minute acquisition, the noise propagation analysis yielded a Signal-to-Noise Ratio (SNR) of ≈ 33.9 for water. This is significantly higher than conventional crystal-based PET, which yields only ≈ 5% DS-LORs and a lower SNR. Reconstructions successfully resolved the NEMA phantom features, including the cold lung insert and hot spheres, particularly when phantom-scattered events were rejected.

Conclusions and future directions: This study confirms that DS-LORs retain sufficient attenuation information to estimate μ-maps, demonstrating the potential for fully CT-less PET imaging. While the current implementation faces limitations like reliance on blank scans and activity-attenuation crosstalk, the high statistics of DS-LORs are a foundation for developing joint reconstruction algorithms aiming towards clinical application.

KEYWORDS

PET imaging, attenuation correction, detector-scattered photons, J-PET, CT-less PET, plastic scintillators, GATE simulation

LIST OF ABBREVIATIONS

AFOV – Axial Field-Of-View
CT – Computed Tomography
DS-LORs – Detector-Scattered Lines Of Response
FBP – Filtered Back-Projection
J-PET – Jagiellonian Positron Emission Tomograph
LOR – Line of Response
MLAA – Maximum Likelihood reconstruction of Attenuation and Activity
NEMA IQ – National Electrical Manufacturers Association Image Quality
PET – Positron Emission Tomography
SNR – Signal-to-Noise Ratio
ST – Scatter Test

INTRODUCTION

Positron emission tomography (PET) enables non-invasive 3D mapping of radiotracer activity by detecting coincident 511-keV annihilation photons, facilitating the in vivo visualisation of metabolic processes [1]. Since the late 1990s, integration of PET with x-ray-computed tomography (CT) in a single gantry has provided high-resolution anatomy and attenuation maps (μ-maps), essential for quantitative reconstruction [2–4]. While CT enhances molecular sensitivity and corrects for photon attenuation, it introduces extra x-ray radiation dose, hardware complexity and risks of misregistration and artifact propagation into PET quantification [5].

These limitations have motivated the exploration of CT-less PET, particularly the challenge of deriving reliable μ-maps without transmission scans. Three main approaches have emerged: (1) emission-only joint estimation (e.g., MLAA) [6, 7], limited by activity-attenuation crosstalk despite time-of-flight mitigation; (2) scatter-informed methods using phantom-scattered coincidences [8], hindered by non-linearity and sensitivity to energy windows and object size; and (3) anatomy-driven μ-map inference from MRI via segmentation or machine learning [9], challenged by bone modelling, implants and cross-site generalisation.

This work introduces a distinct, physics-driven approach tailored to the Jagiellonian positron emission tomograph (J-PET), a plastic-scintillator-based PET scanner characterised by its unique Compton-scattering properties [10–12]. The J-PET system employs long BC-404 scintillator strips in which 511-keV annihilation photons predominantly undergo Compton scattering. Beyond medical imaging applications, the J-PET scanner is also utilised for positronium imaging [13], enabling investigations of discrete symmetry violations in purely leptonic systems through the study of ortho-positronium (o-Ps) decays and the properties of the resulting annihilation photons [14, 15].

Due to the dominance of Compton scattering in plastic scintillators, a substantial fraction of detected events, approximately 50% of all prompts, correspond to detector-scattered lines of response (DS-LORs). These are coincidence events in which one or both of the 511-keV annihilation photons undergo Compton scattering within a plastic scintillator strip and are subsequently registered in a different detector module (Fig. 1.).

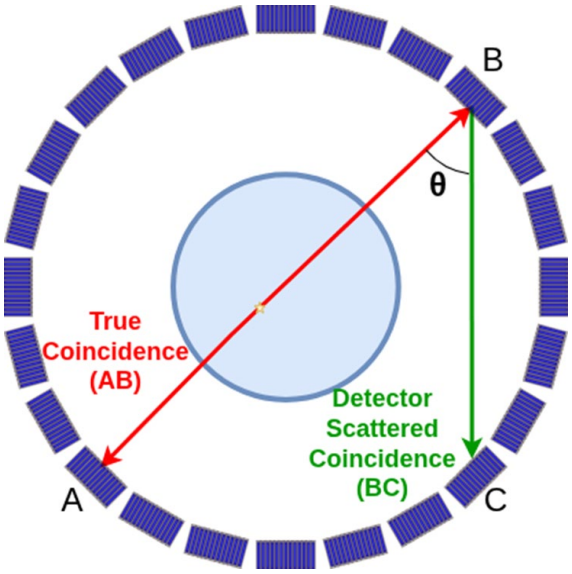

Fig. 1. Schematic of true and detector-scattered lines of response (DS-LORs). In DS-LORs, one or both 511-keV photons undergo compton scattering within a scintillator strip before detection in another module, mispositioning the reconstructed LOR relative to the true annihilation point.

Though typically discarded due to spatial bias, DS-LORs retain attenuation-dependent information: the probability of a photon reaching a detector and scattering into a valid LOR is modulated by tissue along its path. Thus, DS-LORs constitute an intrinsic, transmission-like dataset generated during standard emission imaging, without external sources or anatomical priors.

Leveraging GATE Monte Carlo simulations [16], this study demonstrates that the abundant DS-LORs in J-PET can be repurposed to estimate μ-maps, enabling CT-less, dose-reduced quantitative PET.

METHODS

Modular J-PET Scanner

The modular J-PET scanner (Fig. 2.), developed at Jagiellonian University, employs 312 BC-404 plastic scintillator strips (2.4 cm × 0.6 cm × 50 cm) arranged cylindrically in 24 detection modules [17]. Each module consists of 13 plastic scintillators.

The scanner's 73.9-cm inner diameter and 50-cm axial field-of-view (AFOV) is a prototype of the total-body PET imaging [18, 19]. Dual-ended readout by a matrix of SiPMs (1 × 4) yields a time-of-flight resolution of ≈ 300 ps [17], which corresponds to an axial

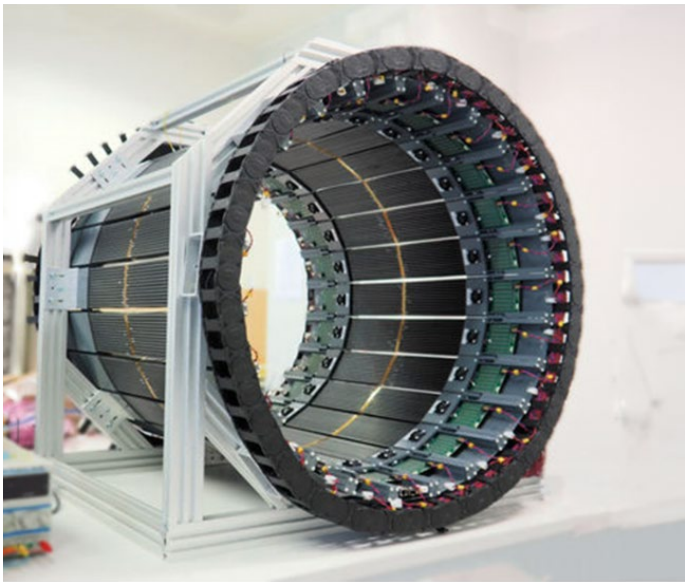

Fig. 2. The modular J-PET scanner prototype developed at Jagiellonian University. This modular architecture enables flexible configuration, high timing precision and efficient detection of photons.

resolution of approximately 2.5 cm. A distinctive feature of J-PET is its high fraction of detector scatterings, which in this study we aim to leverage for the attenuation correction.

Simulation Setup

Simulations were performed using the GEANT4 application for tomographic emission (GATE v9.1) [16]. The PET scanner geometry was modelled to precisely replicate the physical J-PET prototype. Each strip was axially segmented into 200 layers of 2.5-mm thickness to simulate readout along the strip's length.

Two phantom configurations were simulated (Fig. 3.):

- **Uniform phantom:** homogeneous water cylinder (25-cm radius, 80-cm length);
- **NEMA IQ-like Phantom:** A simplified approximation of the NEMA IQ-like phantom, consisting of a water cylinder (11-cm radius, 20-cm height) with a cold lung insert (2.5-cm radius, 0.3 g cm^{-3}) and six hot spheres (10–37-mm diameter, hexagonal arrangement at 5.7-cm radius).

A ^{68}Ge/^{68}Ga source was used, emitting 511 keV back-to-back photon pairs isotropically. For the NEMA IQ-like phantom, activity concentrations were set to 5 kBq/mL in the background water, 20 kBq/mL in the hot spheres (4:1 contrast) and zero in the lung insert.

The digitiser chain incorporated:

- `adderCompton` to sum Compton-scattered energy deposits within the same readout segment;
- readout at a depth of 5 (axial layer level);
- energy blurring with 23.1% FWHM at 200 keV (scaled to 511 keV);
- energy threshold of 50 keV;
- 3-ns-coincidence time window.

Physics processes were modelled using the `emlivermore_polar` list, with production cuts set to 1 m in the world volume to minimise secondary particle generation outside the scanner.

Event Selection for DS-LORs and Triple-Hit Analysis

DS-LORs are identified from time-sorted GATE `Singles` output using a scatter-test metric. For the pair of hits *i* and *j*, the metric is defined as:

$$ST_{i,j} = |\mathbf{r}_i - \mathbf{r}_j| - c \cdot |t_i - t_j|, \quad (1)$$

where $\mathbf{r}_i$ and $\mathbf{r}_j$ are the 3-D interaction positions, t_i and t_j are the detection times and c is the speed of light. True coincidences satisfy $ST_{i,j} > 0$, while detector-scattered events form a sharp peak, at $ST_{i,j} \approx 0$.

To isolate DS-LORs and enable angular analysis (*Angular Distribution of Detector-Scattered LORs*), we focus on triple-hit coincidence events originating from a single annihilation (two 511-keV photons, one unscattered, one scattered in the detector). The following selection criteria were applied:

1. Group all hits by `eventID` to identify interactions from the same annihilation event;
2. Select the three earliest hits in chronological order (expected: one unscattered photon + two interactions from the scattered photon);
3. Compute $ST_{i,j}$ for all three pairwise combinations;
4. Identify the pair with the smallest positive $ST_{i,j}$ as the detector-scattered trajectory (scintillator entry → exit);
5. Form the DS-LOR using the remaining (unscattered) hit and the time-ordered scattered pair (first and second interaction of the scattered photon);
6. Apply a geometric filter: require a minimum sector difference ≥ 1 between the unscattered hit and the scattered pair to exclude intra-module events.

This method robustly isolates inter-module Compton scattering events and provides the true annihilation direction (from the unscattered photon) and the reconstructed DS-LOR (from the scattered path), enabling computation of the signed angular deviation θ (Eq. 2). Note that this triple-hit selection is used specifically for angular distribution analysis; standard DS-LOR reconstruction for μ-map estimation uses dual-hit coincidences with energy and timing constraints.

Angular Distribution of DS-LORs

To characterise the scattering geometry of DS-LORs, we computed the signed angular deviation θ between the true and

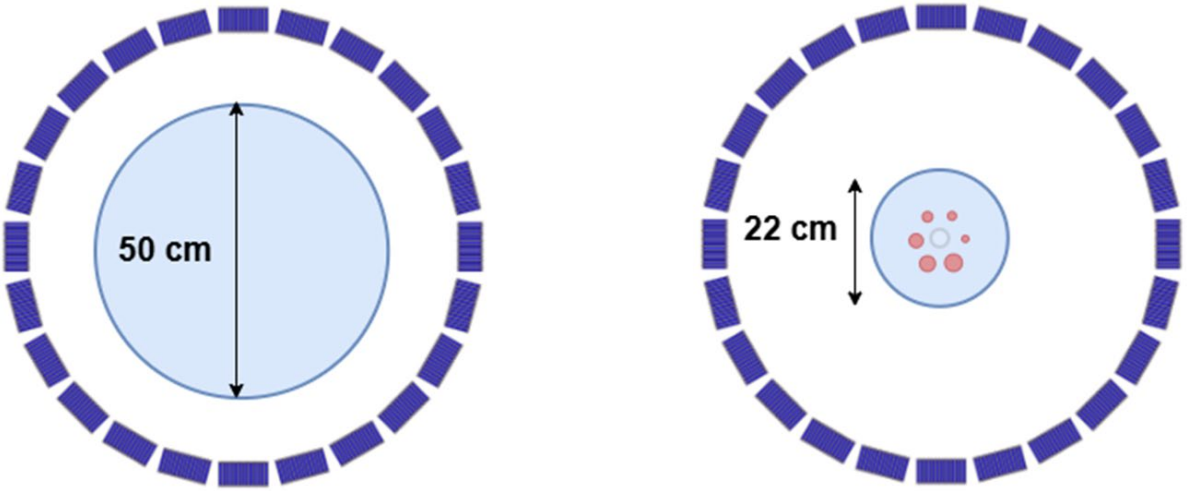

Fig. 3. Transverse schematic of simulated phantoms: (left) uniform water cylinder; (right) NEMA IQ-like phantom with lung insert and six hot spheres (diameters: 10–37 mm).

detector-scattered lines of response, as illustrated in Fig. 1. Two configurations were analysed: an air phantom (no attenuation, equivalent to a blank scan) and a uniform water phantom.

Let $\vec{A}$ and $\vec{B}$ denote the interaction points of the two annihilation photons in the detector. The true LOR direction is defined as

$$\vec{d}_{true} = \vec{A} - \vec{B},$$

and the direction of the detector-scattered LOR (DS-LOR) as

$$\vec{d}_{DS} = \vec{C} - \vec{B},$$

where $\vec{C}$ corresponds to the secondary (scattered) interaction of the photon initially detected in module B. With this convention, $\theta = 0°$ corresponds to forward scattering (i.e., $\vec{d}_{DS}$ is parallel to $\vec{d}_{true}$), consistent with the geometry shown in Fig. 1. and the angular axis in Fig. 4.

The unsigned angle ϕ between the two LORs is given by

$$\phi = \arccos\left(\frac{\vec{d}_{true} \cdot \vec{d}_{DS}}{|d_{true}||d_{DS}|}\right).$$

To establish a continuous angular orientation, the cross product $\vec{d}_{true} \times \vec{d}_{DS}$ is projected onto the axial direction $\hat{n} = [0, 0, 1]$:

$$\text{sign} = \text{sgn}\left((\vec{d}_{true} \times \vec{d}_{DS}) \cdot \hat{n}\right). \quad (2)$$

The signed angle $\theta \in [-180°, 180°)$ is then computed as:

$$\theta = \begin{cases} \phi, & \text{if sgn} \geq 0, \\ -\phi, & \text{if sgn} < 0, \end{cases} \quad (2)$$

where positive angles correspond to counterclockwise rotation around the scanner axis. This definition ensures that $\theta = 0°$ represents forward scattering, and the symmetry of the cylindrical detector is preserved.

Fig. 4. shows the normalised distributions of signed angular deviations for both phantom configurations. Each spectrum was normalised to unit area to allow a direct comparison of angular shapes, independent of the total number of DS-LOR events.

The valley around $\theta = 0°$ reflects the forward-scattering dominance predicted by the Klein–Nishina differential cross-section at 511 keV. In contrast, photons scattered backward deposit only a small fraction of their energy, yielding low detection efficiency at the applied 50 keV energy threshold. The reduced amplitude in the water phantom indicates attenuation-driven suppression of detector scattering at larger scattering angles. This attenuation--dependent modulation of the θ distribution demonstrates that DS--LORs encode medium-dependent photon-transport information, forming a potential basis for CT-less attenuation correction.

Noise Propagation Analysis

The clinical feasibility of reconstructing attenuation maps (μ-maps) from DS-LORs depends on event statistics. We assessed noise for a typical 10-minute scan using Monte Carlo-derived rates and J-PET specifications.

a) Event-rate assumptions

- **Total prompt rate:** 1×10^7 counts/min (trues + scatters + randoms);
- **DS-LOR fraction (J-PET):** 50% of prompts (due to high Compton yield in plastic);
- **DS-LOR fraction (crystal PET):** 5% (due to high photoelectric absorption);
- **Total DS-LORs in 10 min:**
  – J-PET: $0.5 \times 10^7 \times 10 = 5 \times 10^7$
  – Crystal PET: $0.05 \times 10^7 \times 10 = 5 \times 10^6$

b) Noise propagation framework

To evaluate the noise characteristics in the reconstructed

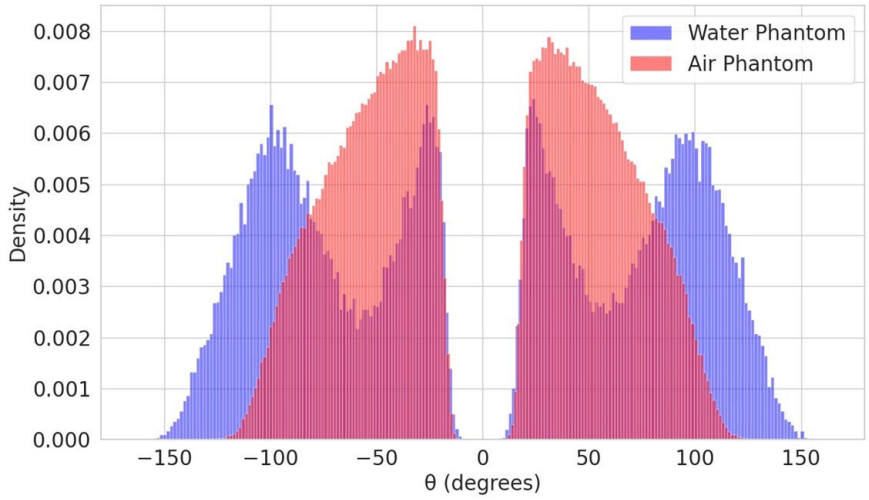

Fig. 4. Signed angular deviation θ between true and DS-LORs for **water (blue)** and **air (orange)** phantoms. θ = 0° corresponds to forward scattering. Each spectrum is normalised to its unit area.

attenuation maps from DS-LORs, we considered a sinogram comprising 120,000 bins, derived from 300 projection angles and 400 radial bins. The noise propagation through the reconstruction process is analysed step-by-step as follows:

1. **Average bin occupancy (J-PET):** This represents the mean number of counts per sinogram bin, calculated by dividing the total number of DS-LOR events (5×10^7) by the total number of bins (1.2×10^5), yielding approximately 417 counts per bin.

$$I_{avg} = \frac{5 \times 10^7}{1.2 \times 10^5} \approx 417 \text{ counts/bin}$$

2. **Projection-space noise (poisson):** Assuming poisson statistics for the counting process, the relative noise in the projection space is the reciprocal of the square root of the average bin occupancy, resulting in about 0.0490 or 4.90% relative uncertainty.

$$\sigma_p = \frac{1}{\sqrt{417}} \approx 0.0490 \text{ (relative)}$$

3. **Reconstructed image noise (FBP, 300 angles):** When reconstructing the image using filtered back-projection (FBP), the noise in the attenuation coefficient (σ_μ) is reduced by the square root of the number of projection angles (300), leading to an absolute noise level of approximately 0.00283 cm^{-1}.

$$\sigma_\mu = \frac{0.0490}{\sqrt{300}} \approx 0.00283 \text{ cm}^{-1}$$

The sinogram bin width is taken as the unit length (Δ = 1 cm). Consequently the line-integral noise σ_y (dimensionless) is divided by this pixel size, giving σ_μ as the physical dimension of a linear attenuation coefficient, [cm^{-1}].

4. **Signal-to-noise ratio** (water, μ_{water} = 0.096 cm^{-1} [20]): The SNR is determined by dividing the attenuation coefficient of water (0.096 cm^{-1}) by the reconstructed image noise, providing a value of about 33.9, which indicates sufficient statistical quality for clinical applications.

$$\text{SNR} = \frac{0.096}{0.00283} \approx 33.9$$

c) Comparison with crystal-based systems

Tab. I. compares J-PET (50% DS-LORs) with conventional crystal PET (5% DS-LORs). J-PET's 10-fold higher DS-LOR yield delivers ~3.2× higher SNR than crystal-based systems with 5% DS-LOR fraction, enabling high-fidelity μ-map estimation in clinical scan times.

RESULTS

The attenuation maps (μ-maps) were reconstructed from DS--LORs using filtered back-projection applied to the ratio of water--to-air sinograms:

$$p(s, \theta) = -\ln\left(\frac{I(s,\theta)}{I_0(s,\theta)}\right),$$

where $I(s, \theta)$ and $I_0(s, \theta)$ are the normalised sinograms from the water and air phantoms, respectively. Here, $p(s, \theta)$ represents the logarithmic attenuation projection, i.e., the line integral of the attenuation coefficient along the path defined by (s, θ):

$$p(s, \theta) = \int u(x,y)\, dl.$$

Two phantom geometries were evaluated:

- **Uniform water phantom (Fig. 5.):** binned into 5 slices (100-mm thickness each), with a 400 × 400 sinogram grid;
- **NEMA IQ-like phantom (Fig. 6.):** binned into 5 slices (12-mm thickness each), same sinogram resolution.

For each phantom, reconstructions were performed with and without rejection of phantom-scattered events using the `comptonPhantom` criteria described in *Materials and methods*. This separation tests whether DS-LORs retain quantitative information when contaminated by object scatter.

Tab. I. Noise performance for a 10-minute scan (120,000 sinogram bins). σ_μ: reconstructed attenuation noise (cm^{-1}); SNR: signal-to-noise ratio in water (μ_{water} = 0.096 cm^{-1}).

METRIC	CRYSTAL PET (5% DS)	J-PET (50% DS)
Total DS-LORs	5×10^6	5×10^7
Avg. counts/bin	41.67	416.67
σ_p (relative)	0.1549	0.0490
σ_μ (cm^{-1})	0.00895	0.00283
SNR (water)	10.7	33.9

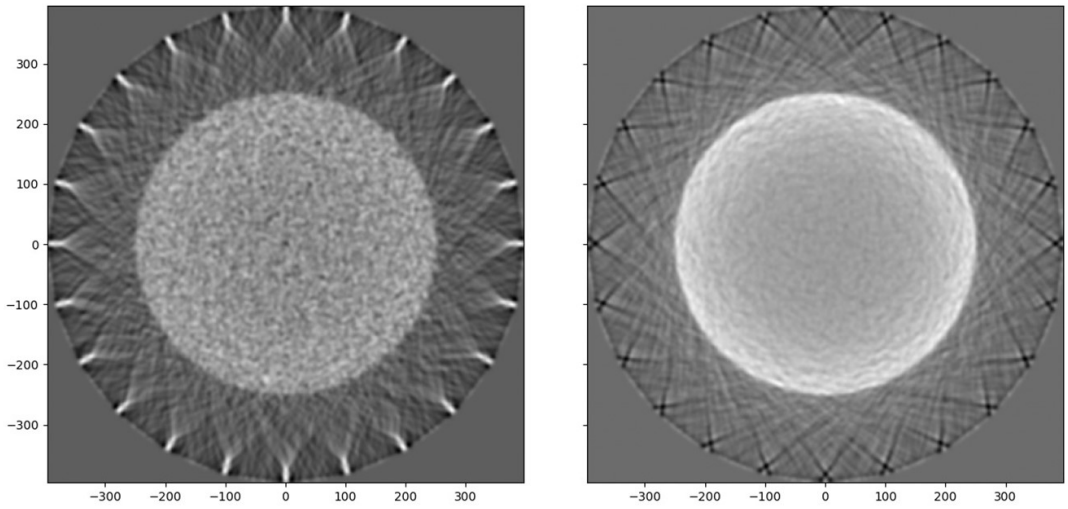

Fig. 5. Filtered back projection (FBP) reconstruction of the uniform water phantom (central slice, z ≈ 0). **Left:** Reconstruction including DS-LORs affected by the phantom scatter. **Right:** Reconstruction excluding phantom-scattered events using the `comptonPhantom` flags. The uniform intensity distribution within the 25-cm radius and the well-defined boundary confirm effective attenuation correction. Notably, cupping artifacts are significantly reduced when phantom scatter is removed.

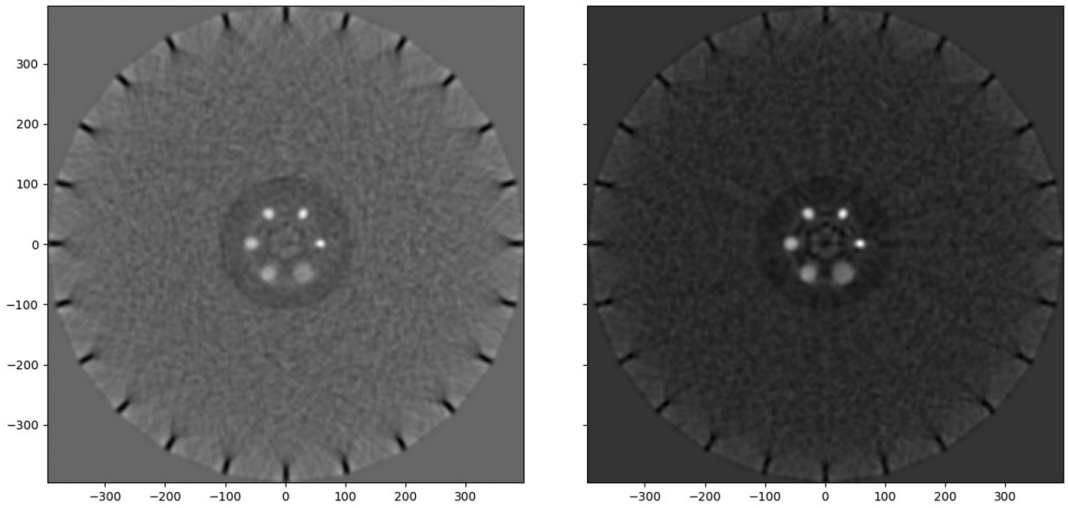

Fig. 6. FBP reconstruction of the NEMA IQ-like phantom (central slice, z ≈ 0). **Left:** With phantom scatter. **Right:** Phantom scatter rejected. The six hot spheres (diameters 10–37 mm) and cold lung insert are clearly resolved. Contrast and boundary definition improve markedly with scatter rejection, confirming that DS-LORs encode spatially varying attenuation.

Both phantoms show consistent improvement in contrast and boundary definition when phantom scatter is rejected. However, even without rejection, DS-LORs produce recognisable attenuation structures. The uniform phantom exhibits only moderate cupping artifact, while the NEMA IQ-like phantom resolves all six spheres and the lung insert despite heterogeneous activity distribution. These results validate DS-LORs as a viable intrinsic transmission source for CT-less attenuation correction in plastic scintillators-based PET.

DISCUSSION

This study demonstrates that detector-scattered coincidences (DS-LORs) can be repurposed for CT-less attenuation correction. Conventionally discarded due to spatial mispositioning, these events are sufficiently abundant in J-PET (reaching ≈ 50% of the prompt rate), to serve as an intrinsic transmission-like source for quantitative attenuation estimation.

The FBP reconstructions (Fig. 5., 6.) successfully recover both uniform and heterogeneous attenuation structures. However, two fundamental limitations need to be addressed.

First, the reconstructed maps are not purely quantitative. They reflect activity-weighted path lengths rather than true linear attenuation coefficients (μ). This activity-attenuation crosstalk arises because the detection probability of DS-LORs depends on the emission distribution, introducing emission-dependent bias into the sinogram. Although the spatial pattern of attenuation is clearly recovered, quantitative μ-values remain systematically biased by activity. Second, our approach requires an air phantom as a blank scan to form $-\ln(I/I_0)$ projections. This works in simulation but fails clinically; no emission-free reference exists in CT-less imaging practice.

These limitations necessitate iterative joint reconstruction. Methods like MLAA (maximum likelihood activity and attenuation) [7, 21] or Bayesian approaches with anatomical priors [22] can simultaneously estimate emission and attenuation from both true and scattered coincidences, eliminating the need for external transmission sources entirely. With J-PET, the statistics of DS-LORs are ample: 50 million events in 10 minutes yield SNR ≈ 34 in water (Tab. I.), enough to regularise this ill-posed problem.

Additional considerations include random coincidence contamination and energy-dependent bias. Using a 3-ns coincidence window and sector filter provide partial suppression, but TOF-based correction will further improve the purity of events. In addition, energy-resolved weighting using deposited energy to infer scatter angle may further refine μ-map accuracy.

CONCLUSIONS

The modular J-PET prototype offers a clear path to experimental validation of utilisingDS-LORs for reconstructing the attenuation map. Hybrid physics-ML pipelines, initialised with FBP μ-maps and refined through learned anatomical priors, could enable real-time CT-less reconstruction. While FBP establishes feasibility, clinically useful quantitative μ-maps will require blank-free, joint estimation of activity and attenuation. Incorporating TOF constraints and energy--resolved weighting should further suppress crosstalk and improve quantitative accuracy.

ACKNOWLEDGEMENT

It is acknowledged that this work was supported by the National Science Centre of Poland through grants MAESTRO no. 2021/42/A/ST2/00423, OPUS no. 2021/43/B/ST2/02150, OPUS24+LAP no. 2022/47/I/NZ7/03112 and SONATA no. 2023/50/E/ST2/00574, the Ministry of Science and Higher Education through grant no. IAL/SP/596235/2023, and the SciMat and qLife Priority Research Areas budget under the program Excellence Initiative – Research University at Jagiellonian University and the European Union within the Horizon Europe Framework Programme (ERC Advanced Grant POSITRONIUM no. 101199807).

We also acknowledge the Polish high-performance computing infrastructure PLGrid (HPC Center: ACK Cyfronet AGH) for providing computer facilities and support within computational grant no. PLG/2024/017688.

REFERENCES

1. Alavi A, Werner T, Stępień E, Moskal P. Unparalleled and revolutionary impact of PET imaging on research and day to day practice of medicine. Bio-Algorithms and Med-Systems. 2021;17(4):203–12. doi: https://doi.org/10.1515/bams-2021-0186.
2. Eubank WB, Mankoff DA, Schmiedl UP, Winter TC 3rd, Fisher ER, Olshen AB, et al. Imaging of oncologic patients: benefit of combined CT and FDG PET in the diagnosis of malignancy. AJR Am J Roentgenol. 1998 Oct;171(4):1103–10.
3. Kinahan PE, Townsend DW, Beyer T, Sashin D. Attenuation correction for a combined 3D PET/CT scanner. Med Phys. 1998 Oct;25(10):2046–53.
4. Beyer T, Townsend DW, Brun T, Kinahan PE, Charron M, Roddy R, et al. A combined PET/CT scanner for clinical oncology. J Nucl Med. 2000 Aug;41(8):1369–79.
5. Blodgett TM, Mehta AS, Laymon CM, Carney J, Townsend DW. PET/CT artifacts. Clin Imaging. 2011 Jan-Feb;35(1):49–63.
6. Rezaei A, Deroose CM, Vahle T, Boada F, Nuyts J. Joint Reconstruction of Activity and Attenuation in Time-of-Flight PET: A Quantitative Analysis. J Nucl Med. 2018 Oct;59(10):1630–5.
7. Nuyts J, Dupont P, Stroobants S, Benninck R, Mortelmans L, Suetens P. Simultaneous maximum a posteriori reconstruction of attenuation and activity distributions from emission sinograms. IEEE Trans Med Imaging. 1999 May;18(5):393–403.

8. Berker Y, Kiessling F, Schulz V. Scattered PET data for attenuation--map reconstruction in PET/MRI. Med Phys. 2014 Oct;41(10):102502.

9. Chen Y, An H. Attenuation Correction of PET/MR Imaging. Magn Reson Imaging Clin N Am. 2017 May;25(2):245–55.

10. Moskal P, Dulski K, Chug N, Curceanu C, Czerwiński E, Dadgar M, et al. Positronium imaging with the novel multiphoton PET scanner. Sci Adv. 2021 Oct 15;7(42):eabh4394.

11. Moskal P, Silarski M, Salabura P, et al. Novel detector systems for the Positron Emission Tomography. Bio-Algorithms and Med-Systems 2011;7(2):73–8. doi: https://doi.org/10.48550/arXiv.1305.5187.

12. Moskal P, Kumar D, Sharma S, Beyene EY, Chug N, Coussat A, et al. Nonmaximal entanglement of photons from positron-electron annihilation demonstrated using a plastic PET scanner. Sci Adv. 2025 May 2;11(18):eads3046. doi: https://doi.org/10.1126/sciadv.ads3046.

13. Moskal P, Stępień E. Positronium as a biomarker of hypoxia. Bio-Algorithms and Med-Systems 2021;17(4):311–9. https://doi.org/10.1515/bams-2021-0189.

14. Moskal P, Gajos A, Mohammed M, Chhokar J, Chug N, Curceanu C, et al. Testing CPT symmetry in ortho-positronium decays with positronium annihilation tomography. Nat. Commun. 2021;12:5658.

15. Moskal P, Czerwiński E, Raj J, Bass SD, Beyene EY, Chug N, et al. Discrete symmetries tested at 10-4 precision using linear polarization of photons from positronium annihilations. Nat Commun. 2024 Jan 2;15(1):78.

16. Jan S, Santin G, Strul D, Staelens S, Assié K, Autret D, et al. GATE: a simulation toolkit for PET and SPECT. Phys Med Biol. 2004 Oct 7;49(19):4543–61.

17. Moskal P, Kisielewska D, Curceanu C, Czerwiński E, Dulski K, Gajos A, et al. Feasibility study of the positronium imaging with the J-PET tomograph. Phys Med Biol. 2019 Mar 7;64(5):055017.

18. Niedźwiecki S, Białas P, Curceanu C, Czerwiński E, Dulski K. J-PET: A new technology for the whole-body PET imaging. Acta Phys. Polon. B. 2017;48:1567.

19. Moskal P, Stępień EŁ. Prospects and Clinical Perspectives of Total-Body PET Imaging Using Plastic Scintillators. PET Clin. 2020 Oct;15(4):439–52.

20. Hubbell J, Seltzer S. Tables of X-Ray Mass Attenuation Coefficients and Mass Energy-Absorption Coefficients 1 keV to 20 MeV for Elements Z = 1 to 92 and 48 Additional Substances of Dosimetric Interest. [Internet]. Available from: http://physics.nist.gov/PhysRefData/XrayMassCoef/cover.html.

21. Rezaei A, Defrise M, Bal G, Michel C, Conti M, Watson C, et al. Simultaneous reconstruction of activity and attenuation in time-of-flight PET. IEEE Trans Med Imaging. 2012 Dec;31(12):2224–33.

22. Berker Y, Li Y. Attenuation correction in emission tomography using the emission data – A review. Med Phys. 2016 Feb;43(2):807–32.